Spacecraft Observations and Analytic Theory of Crescent-Shaped Electron Distributions in Asymmetric Magnetic Reconnection

J. Egedal,[1] A. Le,[2] W. Daughton,[2] B. Wetherton,[1] P. A. Cassak,[3] L.-J Chen,[4] B. Lavraud,[5] R. B. Torbert,[6] J. Dorelli,[4] D. J. Gershman,[4] and L. A. Avanov[4]

[1]*Department of Physics, University of Wisconsin–Madison, Madison, Wisconsin 53706, USA*
[2]*Los Alamos National Laboratory, Los Alamos, New Mexico 87545, USA*
[3]*Department of Physics and Astronomy, West Virginia University, Morgantown, West Virginia 26506, USA*
[4]*Heliophysics Science Division, NASA Goddard Space Flight Center, Greenbelt, Maryland 20771, USA*
[5]*Institut de Recherche en Astrophysique et Planétologie, Université de Toulouse, Toulouse, France, and Centre National de la Recherche Scientifique, UMR 5277, Toulouse, France*
[6]*University of New Hampshire, Durham, New Hampshire 03824, USA*

(Received 20 July 2016; published 24 October 2016)

Supported by a kinetic simulation, we derive an exclusion energy parameter $\mathcal{E}_X$ providing a lower kinetic energy bound for an electron to cross from one inflow region to the other during magnetic reconnection. As by a Maxwell demon, only high-energy electrons are permitted to cross the inner reconnection region, setting the electron distribution function observed along the low-density side separatrix during asymmetric reconnection. The analytic model accounts for the two distinct flavors of crescent-shaped electron distributions observed by spacecraft in a thin boundary layer along the low-density separatrix.

DOI: 10.1103/PhysRevLett.117.185101

Magnetic reconnection converts magnetic energy into kinetic energy of ions and electrons both during solar flare events [1] and reconnection observed *in situ* in Earth's magnetosphere [2]. Common for most theoretical models of reconnection is an emphasis on the dynamics of the electrons and their role in breaking the *frozen-in* conditions for the electron fluid, permitting the magnetic field lines to change topology and release the stored magnetic stress in naturally occurring plasmas [3]. NASA's new magnetospheric multiscale (MMS) mission is specially designed to address this question, as it can detect *in situ* possible mechanisms including electron inertia, pressure tensor effects, and anomalous dissipation for decoupling the electron motion from the magnetic field lines [4].

The identification of diffusion regions in the vast data set now being recorded by MMS relies in part on numerical and theoretical models for distinct signatures of the reconnection region and the associated separatrix structure. Recent simulations of crescent-shaped electron distributions [5,6] have been proposed as a robust signature to find diffusion regions. The crescents are observed in two flavors: perpendicular and parallel to the magnetic field [7]. The perpendicular crescent shapes are predicted theoretically in Refs. [8,9], using 1D reasoning valid near the X line, with electrons interacting strongly with an normal electric field E_N [in the N direction; see Figs. 1(a) and 1(b)].

Considering 2D geometries, here we provide a general derivation which accounts for the occurrence of both the perpendicular and parallel crescents. Only high-density (magnetosheath) particles with sufficient energy can cross the diffusion region to the low-density (magnetospheric) inflow region. Thus, the diffusion region acts like a Maxwell demon, allowing only the most energetic particles across. This provides an explanation for why the distributions are crescent-shaped rather than filled in at lower energies. The requirement of having a sufficient energy is here quantified in terms of what we call the exclusion energy $\mathcal{E}_X$. As such, magnetosheath electrons with kinetic energies $\mathcal{E} > \mathcal{E}_X$ can access magnetic field lines on the magnetospheric side of the separatrix, exiting the region along the separatrix with nearly perfectly circular perpendicular motion. The parallel streaming and the absence of electrons with $\mathcal{E} < \mathcal{E}_X$ yields the parallel crescent-shaped distributions, and their origin is thus consistent with the analysis in Ref. [7]. However, contrary to the models applicable near the X line [8,9], we find that the perpendicular crescents along the separatrix are comprised of well-magnetized electrons with nearly circular perpendicular orbit motion.

On October 16, 2015, NASA's MMS mission had an encounter with an active reconnection region at the dayside magnetopause. The location of the encounter is sketched by the red rectangle in Fig. 1(a), as was established by the analysis in Ref. [7]. Based in part on the recorded time series of the magnetic fields and ion flows, it was concluded that three of the four MMS spacecraft (MMS1, MMS2, and MMS3) passed the diffusion region on its northern side, while MMS4 passed it on the southern side. The four spacecraft all recorded similar structures, and here we consider data obtained by MMS3 and MMS4. The paths near the separatrix of these two spacecraft are sketched in Fig. 1(b), crossing from the low plasma density magnetosphere into the reconnection exhausts, in which the plasma

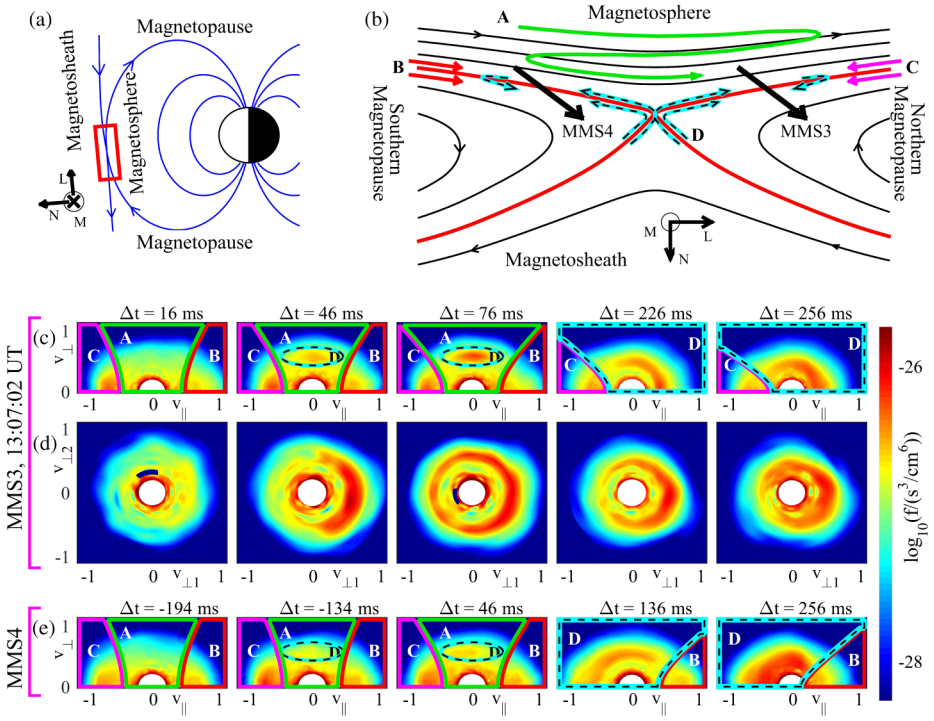

FIG. 1. (a) Schematic illustration of the reconnection region encountered by the MMS mission on October 16, 2015. (b) The trajectories of the MMS spacecraft were determined in Ref. [7] and are indicated by the black arrows. In addition, distinct orbit types are labeled. (c)–(e) Electron distribution function recorded during the separatrix crossing by MMS3 and MMS4, respectively. Times are given relative to 13:07:02.000 UT. The velocity axes are normalized by $v_0 = 10^7$ m/s, and all distributions are computed from the full 3D MMS measurements. In (c) and (e), $\bar{f}(v_\parallel, v_\perp)$ are gyro-averaged distributions, and regions of distinct orbit types are labeled consistently with the trajectories in (b). The data in (d) are cuts of the full 3D electron distributions at $v_\parallel = 0$.

is mainly provided by the much higher densities of the magnetosheath [10].

The distinct types of electron trajectories indicated in Fig. 1(b) are important to the structures in the electron distribution function. Passing electrons, labeled **B** and **C**, stream into the reconnection region along magnetic field lines and do not change the signs of their magnetic field aligned (parallel) velocity as they pass through the region. The magnetic mirror force $-\mu\nabla_\parallel B$ [11] and the acceleration potential $\Phi_\parallel = \int_x^\infty E_\parallel dl$ of Ref. [12] trap a significant fraction of the electron population, characterized by bounce orbits illustrated by the green line labeled **A**. During the course of several bounce motions, they convect slowly with the magnetic field lines towards the reconnection separatrix. The basis of this kinetic electron behavior is analogous to that of symmetric reconnection [13–15], but for asymmetric reconnection trapping is most significant in the low-density magnetospheric inflow [16]. Trajectories of magnetosheath electrons near the separatrix (including their possible reflection back toward the X line) are schematically illustrated by the cyan-black dashed lines labeled **D** in Fig. 1(b).

The distribution functions displayed in Figs. 1(c)–1(e) are calculated based on the full 3D electron data recorded by the Fast Plasma Investigation [17] onboard MMS3 and MMS4 for selected time points Δt relative to 13:07:02.000 UT. In the following, we denote gyro-averaged distributions by $\bar{f}$. The distributions $\bar{f}(v_\parallel, v_\perp)$ in Figs. 1(c) and 1(e) are obtained by first rotating the "raw" 3D electron distributions into a coordinate system $(v_\parallel, v_{\perp 1}, v_{\perp 2})$ aligned with the direction of the measured magnetic field. Like in Ref. [7], $v_{\perp 1}$ is in the direction of $(\mathbf{b} \times \mathbf{v}) \times \mathbf{b}$ (where $\mathbf{b}$ and $\mathbf{v}$ are unit vectors of the magnetic field and the electron velocity moment, respectively), while $v_{\perp 2}$ is in the direction of $-\mathbf{v} \times \mathbf{b}$. Furthermore, with $v_\perp = \sqrt{v_{\perp 1}^2 + v_{\perp 2}^2}$, values of $\bar{f}(v_\parallel, v_\perp)$ are then computed as the average of $f(v_\parallel, v_{\perp 1}, v_{\perp 2})$ over the azimuthal gyroangle $\phi = \tan^{-1}(v_{\perp 2}/v_{\perp 1})$.

We first consider $\bar{f}(v_\parallel, v_\perp)$ of MMS3 in Fig. 1(c) for $\Delta t = 16$ ms. Corresponding to the orbit classification in Fig. 1(b), the regions of trapped electrons are labeled **A**, while the regions of passing electrons are labeled by **B** and **C**. Naturally, at locations inside the magnetospheric inflow, both flavors (parallel and antiparallel) of passing electrons are present along the full length of the magnetic field lines [16] and are thus observed by both MMS3 and MMS4. The trapped passing boundaries are obtained based on the local magnetic field and by estimating $\Phi_\parallel$ (covering a range of 45–130 V) by methods given in Ref. [18]. In agreement with Refs. [16,19], this is evidence that the strong parallel electron heating noted in Fig. 3(i) of Ref. [7] is mainly due to energization by $\Phi_\parallel$.

The distributions in Fig. 1(c) for $\Delta t = 46$, 76 ms are similar to that at $\Delta t = 16$ ms, except that these include an additional feature within the trapped region. We mark this feature **D**, as it is caused by energetic magnetosheath electrons penetrating across the separatrix to this location in the magnetospheric inflow. As MMS3 progresses towards the separatrix, $\bar{f}(v_\parallel, v_\perp)$ continues to change. At times $\Delta t = 226$, 256 ms, the regions of incoming passing electrons with $v_\parallel > 0$ [labeled **B** in the $\Delta t = 16$, 46, 76 ms plots in Fig. 1(c)] are now dominated by pitch angle mixed magnetosheath electrons streaming out along the separatrix from the reconnection region. These magnetosheath electrons are, naturally, also subject to parallel acceleration (deceleration) by $\Phi_\parallel$ and the mirror force, such that a fraction of these will be reflected back toward the diffusion region. Because of

their larger density, the magnetosheath electrons dominate the full area in $(v_\parallel, v_\perp)$ space labeled **D**, previously occupied by trapped electrons and region **B** passing electrons.

The distributions in Fig. 1(d) are cuts through $f(v_\parallel, v_{\perp 1}, v_{\perp 2})$ with $v_\parallel = 0$. For $\Delta t = 76$, 226 ms, complete rings in the $(v_{\perp 1}, v_{\perp 2})$ plane are clearly visible. Meanwhile, at $\Delta t = 46$ ms, the ring is incomplete and only a crescent is observed. For this location, the recorded magnetic field is relatively strong, $B = 17.8$ nT, corresponding to a Larmor radius for the typical crescent electrons of less than 2 km. As shown in Fig. 1(e), the distributions recorded by MMS4 are similar to those of MMS3. However, the main and key difference (also discussed in Refs. [7,9]) is the reversed $v_\parallel$ sign of the $(v_\parallel, v_\perp)$ crescent for $\Delta t = 136$ ms in Fig. 1(e). This is consistent with MMS4 crossing into the southern outflow, such that the $v_\parallel < 0$ passing electrons (region **C**) are eliminated in favor of magnetosheath electrons streaming southward, away from the diffusion region.

To explore the dynamics shaping the electron distribution function, we consider the trajectory in Fig. 2(a) calculated using the magnetic and electric fields of a fully kinetic simulation (to be further described below). This electron enters the reconnection region on a trapped trajectory originating in the magnetosheath. It then travels into the diffusion region and exits on the magnetospheric side of the separatrix. Only later does it reach the reconnection exhaust from the magnetospheric side. Apart from the electron's brief encounters with the diffusion region, it is well magnetized with $\kappa^2 = \min(R_B/\rho_l) \gg 1$. Here R_B is the radius of curvature of the magnetic field, ρ_l is the Larmor radius of the electrons, and κ is evaluated where R_B/ρ_l is minimal along the electron trajectory [20,21]. Thus, the regions of chaotic unmagnetized electron dynamics in Fig. 2(a) are identified by the red areas where $\sqrt{\rho_l/R_B} > 0.25$ [11,22].

The above observations motivate a model for the electron dynamics as sketched in Fig. 2(b), where the electron motion outside the chaotic regions is described by the guiding center approximation. For 2D geometries, the canonical momentum in the out-of-plane (M) direction of the guiding centers $P_{M,g} = qA_M + mv_\parallel B_M/B$ is a constant of the guiding center motion. Here A_M is the out-of-plane component of the magnetic vector potential, with the reconnection X line characterized by the value $A_{M,x}$ observed at the saddle point in the profile of A_M. Upstream and close to the separatrix, B_M is small so that $P_{M,g} \simeq qA_M$, and it follows that guiding centers are locked to contours of constant A_M.

A quantitative condition required for magnetosheath electrons to jump to the magnetospheric inflow region is obtained through the use of the canonical momentum $P_M = qA_M + mv_M$ of the full electron motion. This quantity is a constant of motion throughout the cross section, including the chaotic orbit region. Variations in mv_M determine the orbit size and allow the Fig. 2(a) electron to move off its particular A_M contour by the amount $\Delta A_M = m\Delta v_M/q$.

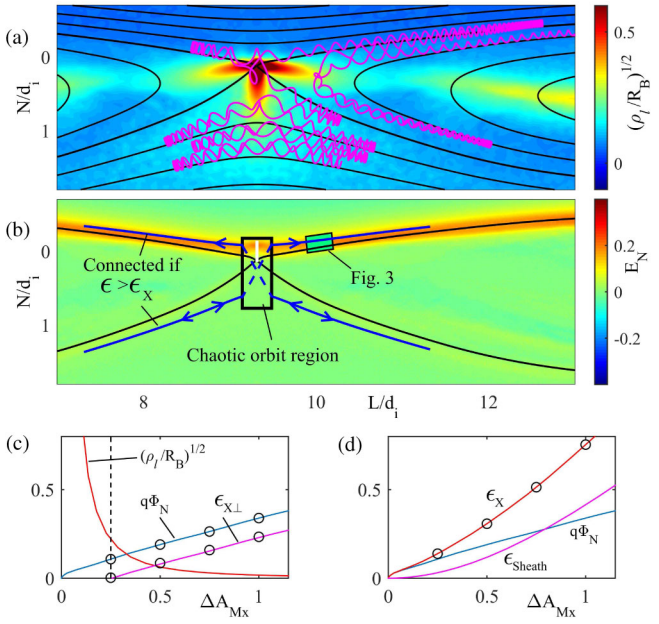

FIG. 2. (a) Trapped magnetosheath electrons propagating across the diffusion region into the magnetospheric inflow. Nongyrotropic regions ($\sqrt{\rho_l/R_B} > 0.25$) are identified by the background color. (b) Guiding center trajectories are characterized by $A_M = \text{const}$, and electrons with $\mathcal{E} > \mathcal{E}_X$ may jump across the diffusion region. The color contours document the strong E_N electric fields along the separatrix. (c) $q\Phi_N$ is a measure of the electron energization, obtained by integrating E_N along the white line in (b). In areas of no pitch angle mixing [for $(\rho_l/R_B)^{1/2} < 0.25$], the energization $\mathcal{E}_{X\perp}$ is purely perpendicular. (d) $\mathcal{E}_{\text{sheath}}$ of Eq. (2) and energization by $q\Phi_N$ add to provide the minimum kinetic energy $\mathcal{E}_X$ of sheath electrons in the magnetospheric inflow. In (c) and (d), values are normalized by mc^2, and those used for computing the distributions in Fig. 3(d) are marked by circles.

Thus, a magnetosheath electron with $P_{M,g} = qA_M$ can cross the separatrix only if the orbit permits a variation

$$\Delta A_{Mx} \equiv A_M - A_{M,x}. \tag{1}$$

This requires an initial minimum kinetic energy in the magnetosheath given by

$$\mathcal{E}_{\text{sheath}} = \frac{q^2(\Delta A_{Mx})^2}{2m}. \tag{2}$$

Magnetosheath electrons passing through the diffusion region are energized by the strong E_N electric field shown in Fig. 2(b), characterized by $q\Phi_N$ in Fig. 2(c), with $\Phi_N = -\int_0^{N(\Delta A_{Mx})} E_N dN$ evaluated along a cut starting at the X line [short white line in Fig. 2(b)]. The minimum kinetic energy is then given by $\mathcal{E}_X = q\Phi_N + \mathcal{E}_{\text{sheath}}$, where the $\mathcal{E}_{\text{sheath}}$ contribution dominates for $\Delta A_{Mx} > 0.8$ [see Fig. 2(d)]. Although E_N is in the perpendicular direction, for $\sqrt{\rho_l/R_B} > 0.25$ pitch angle mixing causes the heating to be approximately uniform in all directions. Meanwhile, for $\sqrt{\rho_l/R_B} < 0.25$ there is no pitch angle mixing such that a part of the energization $\mathcal{E}_{X\perp}$, identified in Fig. 2(c), is

guaranteed to be observed in the perpendicular direction after the electron leaves the diffusion region. Thus, any magnetosheath electron reaching sufficiently deep into the magnetospheric inflow will have a minimum perpendicular energy given by $\mathcal{E}_{X\perp}$.

We may now derive a simple model for the drift kinetic [23] guiding center distribution $\bar{f}_g(\mathbf{x}_g, v_\parallel, v_\perp)$ of magnetosheath electrons on the magnetospheric side of the separatrix. Consistent with the simulation, we assume that the chaotic region is characterized by a Maxwellian distribution $f_{\rm xline}(\mathcal{E})$. Using Liouville mapping of the phase density ($df/dt = 0$), it follows that

$$\bar{f}_g \simeq f_{\rm xline}(\mathcal{E} - q\Phi_N) H(\mathcal{E} - \mathcal{E}_X) H(\mathcal{E}_\perp - \mathcal{E}_{X\perp}), \quad (3)$$

where $H(\mathcal{E})$ is the Heaviside step function. The heating by $q\Phi_N$ is included by evaluating $f_{\rm xline}$ at $\mathcal{E} - q\Phi_N$.

We note that the structure of $E_\parallel$, responsible for the $T_{e\parallel}$ heating of the inflow (of magnitude $e\Phi_\parallel$), will cause parallel cooling [of magnitude $e(\Phi_\parallel - \Phi_{\parallel,\rm xline})$] as the magnetosheath electrons stream away from the X line. In the inner reconnection region, this effect is small and is not included in Eq. (3).

To validate the model in Eq. (3), we consider a kinetic simulation performed with the VPIC code [24] using asymptotic plasma parameters identical to those of Ref. [7]. Here, however, the initial plasma current is carried by a modified Harris sheet [25]. The reconnecting magnetic field and background temperatures vary as $\tanh(N/d_i)$ (d_i based on the magnetosheath density), and the density profile is adjusted to ensure a magnetohydrodynamic pressure balance. The simulation is periodic in L and has conducting boundaries in N, with a total size of 4032×4032 cells $= 20d_i \times 20d_i$. Separate populations of magnetosheath ($N > 0$) and magnetosphere ($N < 0$) particles with different numerical weights are loaded, so that plasma mixing may be tracked over time [26] and so that both regions are resolved with 400 particles per cell per species. Other simulation parameters are a mass ratio of $m_i/m_e = 400$ and $\omega_{pe}/\omega_{ce} = 1.5$ (based on the magnetosheath field and density).

Particle distributions are computed at time $t = 30/\omega_{ci}$, when reconnection has reached a quasisteady state, and as indicated in Fig. 2(b), we use electron data collected $0.7d_i$ away from the X line along the separatrix. The data include only electrons originating from the magnetosheath side and are collected as a function of ΔA_{Mx} for four locations within a narrow region reaching ρ_c from the separatrix into the magnetospheric inflow. Here ρ_c is the characteristic Larmor radius of a typical crescent electron (with relativistic momentum $m\gamma v \simeq mc$). Figure 3(a) shows the sequence of the full distributions integrated over the parallel velocity $f_\perp = \int f(\mathbf{x}, \mathbf{v}) dv_\parallel$, revealing crescent-shaped and ring distributions qualitatively consistent with the MMS observations. Meanwhile, Fig. 3(b) shows the sequence of distributions also integrated over the parallel velocity $f_{g\perp}(\mathbf{x}_g, \mathbf{v}_\perp) = \int f_g(\mathbf{x}_g, \mathbf{v}) dv_\parallel$ but now with the numerical electrons binned as a function of their guiding center locations. As such, $f_g(\mathbf{x}_g, \mathbf{v})$ is the distribution of guiding centers, defined without approximation through $f_g(\mathbf{x}_g, \mathbf{v}) \equiv f(\mathbf{x}_g - \boldsymbol{\rho}, \mathbf{v})$, where the direction of the vector $\boldsymbol{\rho}(\phi) = m\mathbf{v} \times \mathbf{B}/(qB^2)$ is a function of the gyrophase ϕ. The $f_{g\perp}$ distributions are characterized by nearly perfect circles in a frame slightly off-centered from the origin by the $E \times B$ drift; in this frame, these crescent electrons follow nearly perfectly circular perpendicular gyro-orbits, and $f_{g\perp}(\mathbf{x}, \mathbf{v}_\perp)$ is nearly independent of ϕ. Consistent with the MMS data, the

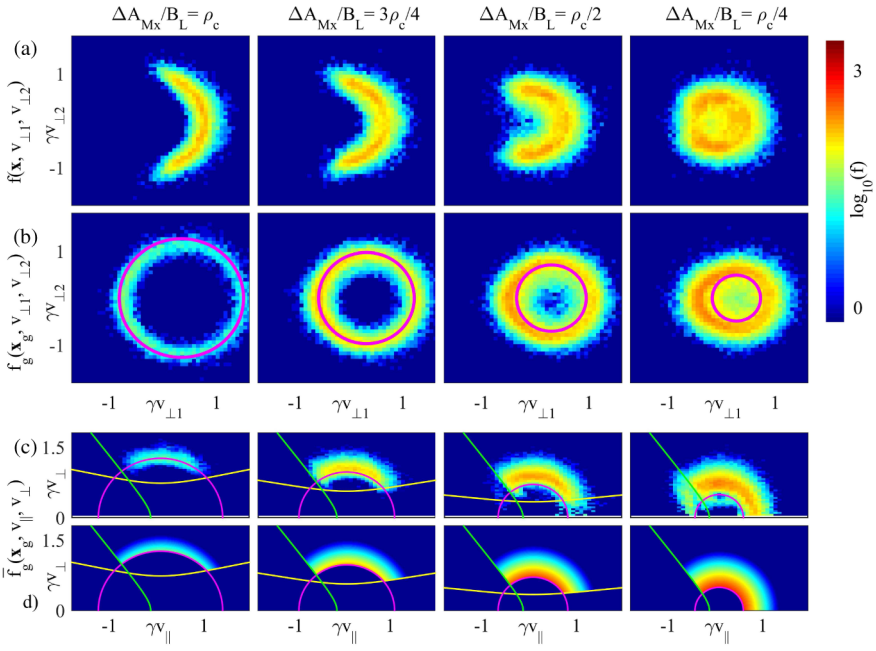

FIG. 3. (a),(c) Rows of distributions for magnetosheath electrons collected from the location in Fig. 2(b) as a function of ΔA_{Mx}. Row (a) shows the local distribution $f(\mathbf{x}, v_{\perp 1}, v_{\perp 2}) = \int f(\mathbf{x}, \mathbf{v}) dv_\parallel$, while row (b) is calculated based on the location of the electrons' guiding centers $f_g(\mathbf{x}_g, v_{\perp 1}, v_{\perp 2}) = \int f_g(\mathbf{x}_g, \mathbf{v}) dv_\parallel$. In (b), the magenta lines show the predicted cutoff energy $\mathcal{E}_X$ at values marked in Fig. 2(d), shifted by the $E \times B$ drift. Rows (c) and (d) display $\bar{f}_g(v_\parallel, v_\perp)$ obtained from the simulation data and Eq. (3), respectively. Again, the magenta lines represent the total cutoff energy $\mathcal{E}_X$, while the yellow lines are the perpendicular cutoff energy $\mathcal{E}_{X\perp}$; both are calculated relativistically based on the values indicated in Fig. 2(c). The green lines mark the boundary to the velocity region of incoming passing magnetosphere electrons, calculated based on the local values of B and $\Phi_\parallel$ [14].

characteristic energies of these ring distributions decrease as the separatrix is approached from the magnetospheric side.

The gyro-averaged distributions of guiding centers $\bar{f}_g(\mathbf{x}_g, v_\parallel, v_\perp)$ in Fig. 3(c) are also compiled from the simulation particle data, where $v_\perp = (v_{\perp 1}^2 + v_{\perp 2}^2)^{1/2}$ is evaluated in the frame of the $E \times B$ drift. The exclusion energies $\mathcal{E}_X$ of Fig. 2(d) are shown by the magenta lines, accurately predicting the lower-energy bound of the numerical distributions. The matching distributions in Fig. 3(d) are obtained from Eq. (3), based on values of $q\Phi_N$, $\mathcal{E}_{X\perp}$, and $\mathcal{E}_X$ marked in Figs. 2(c) and 2(d). The combination of the exclusion energies reproduces the behavior of the $(v_{\perp 1}, v_{\perp 2})$-ring distributions with $v_\parallel \simeq 0$, evolving into crescent-shaped $\bar{f}_g(v_\parallel, v_\perp)$ distributions for locations very close to the separatrix, $\Delta A_{Mx}/B_L < \rho_c/2$. We have verified that the model distribution in Eq. (3) is applicable along the separatrix of the full simulation domain, excluding only the region in Fig. 2(b) where the electrons are unmagnetized.

It is evident from Figs. 3(b)–3(d) how $\mathcal{E}_X$ rapidly increases with ΔA_{Mx}, practically eliminating all electron guiding centers for $\Delta A_{Mx} > B_L \rho_c$. However, the actual electron location is displaced from the guiding center $\mathbf{x} = \mathbf{x}_g - \boldsymbol{\rho}$. Depending on ϕ, this allows electrons to penetrate up to an additional ρ_c into the magnetospheric inflow. As the separatrix is approached from the magnetopause inflow, the first magnetosheath electrons to be observed are those with ϕ placing their guiding centers closer to the separatrix. As such, the crescent distributions are a manifestation of the diamagnetic drifts associated with the rapidly changing pressure of the magnetosheath electrons at the magnetopause-exhaust separatrix.

In summary, we have extended the analysis of the MMS electron data of Ref. [7] and shown that the observed parallel heating of the magnetospheric inflow is consistent with the trapping model of Refs. [13,14]. Furthermore, the $(v_\parallel, v_\perp)$-crescent distribution encountered by MMS can be accounted for by extending the electron dynamics of the trapping model to include magnetosheath electrons penetrating into the magnetosphere. Here the cutoff energy $\mathcal{E}_X$ forbids electrons with insufficient diffusion region orbit size to reach into the magnetospheric inflow. The profile of $\mathcal{E}_X$ depends strongly on the distance from the separatrix, where the chaotic region works like a *Maxwell demon*, letting only the most energetic magnetosheath electrons pass to the magnetospheric side. The perpendicular crescent-shaped distributions are formed due to the spatial gradients imposed by $\mathcal{E}_X$. They are a direct manifestation of the diamagnetic drift of well-magnetized magnetosheath electrons in a boundary layer with a width of about an electron Larmor radius all along the low-density separatrix.

J. E. acknowledges the support by the National Science Foundation (NSF) Geospace Environment Modeling Grant No. 1405166, P. A. C. was supported by NASA Grants No. NNX16AF75G and No. NNX16AG76G, B. L. was supported by Centre national de la recherche scientifique (CNRS) and Centre national d'études spatiales (CNES), while A. L. acknowledges NASA Grant No. NNX14AL38G, and simulations used NASA High End Computing program and Los Alamos National Laboratory IC resources.

[1] S. Krucker, H. S. Hudson, L. Glesener, S. M. White, S. Masuda, J. P. Wuelser, and R. P. Lin, Astrophys. J. **714**, 1108 (2010).
[2] M. Øieroset, T. Phan, M. Fujimoto, R. P. Lin, and R. P. Lepping, Nature (London) **412**, 414 (2001).
[3] J. W. Dungey, Philos. Mag. **44**, 725 (1953).
[4] J. L. Burch, T. E. Moore, R. B. Torbert, and B. L. Giles, Space Sci. Rev. **199**, 5 (2016).
[5] M. Hesse, N. Aunai, D. Sibeck, and J. Birn, Geophys. Res. Lett. **41**, 8673 (2014).
[6] L.-J. Chen, M. Hesse, S. Wang, N. Bessho, and W. Daughton, Geophys. Res. Lett. **43**, 2405 (2016).
[7] J. L. Burch *et al.*, Science **352**, 2939 (2016).
[8] N. Bessho, L.-J. Chen, and M. Hesse, Geophys. Res. Lett. **43**, 1828 (2016).
[9] M. A. Shay, T. D. Phan, C. C. Haggerty, M. Fujimoto, J. F. Drake, K. Malakit, P. A. Cassak, and M. Swisdak, Geophys. Res. Lett. **43**, 4145 (2016).
[10] P. A. Cassak and M. A. Shay, Phys. Plasmas **14**, 102114 (2007).
[11] B. Lavraud *et al.*, Geophys. Res. Lett. **43**, 3042 (2016).
[12] J. Egedal, W. Daughton, J. F. Drake, N. Katz, and A. Le, Phys. Plasmas **16**, 050701 (2009).
[13] J. Egedal, M. Øieroset, W. Fox, and R. P. Lin, Phys. Rev. Lett. **94**, 025006 (2005).
[14] J. Egedal, W. Fox, N. Katz, M. Porkolab, M. Øieroset, R. P. Lin, W. Daughton, and J. F. Drake, J. Geophys. Res. **113**, A12207 (2008).
[15] J. Egedal, A. Le, and W. Daughton, Phys. Plasmas **20**, 061201 (2013).
[16] J. Egedal, A. Le, P. L. Pritchett, and W. Daughton, Phys. Plasmas **18**, 102901 (2011).
[17] C. Pollock *et al.*, Space Sci. Rev. **199**, 331 (2016).
[18] J. Egedal, A. Le, N. Katz, L. J. Chen, B. Lefebvre, W. Daughton, and A. Fazakerley, J. Geophys. Res. **115**, A03214 (2010).
[19] D. B. Graham *et al.*, Geophys. Res. Lett. **43**, 4691 (2016).
[20] T. Birmingham, J. Geophys. Res. **89**, 2699 (1984).
[21] J. Buchner and L. Zelenyi, J. Geophys. Res. **94**, 11821 (1989).
[22] A. Le, J. Egedal, O. Ohia, W. Daughton, H. Karimabadi, and V. S. Lukin, Phys. Rev. Lett. **110**, 135004 (2013).
[23] R. M. Kulsrud, *MHD Description of Plasma* (North-Holland, New York, 2000), Vol. 1.
[24] K. Bowers, B. Albright, L. Yin, W. Daughton, V. Roytershteyn, B. Bergen, and T. Kwan, J. Phys. Conf. Ser. **180**, 012055 (2009).
[25] V. Roytershteyn, W. Daughton, H. Karimabadi, and F. S. Mozer, Phys. Rev. Lett. **108**, 185001 (2012).
[26] W. Daughton, T. Nakamura, H. Karimabadi, V. Roytershteyn, and B. Loring, Phys. Plasmas **21**, 052307 (2014).